

Technical Report for Laboratory Exercise 1
Applied 2-D Photoelastic Analysis

Author (Lead Author): *Gupta, Ankit*

Sections Authored: *Cover Page, Introduction, and Theory*

Co-author: *Eden, Jake*

Sections Authored: *Methods and Materials and Applications*

Co-author: *Sipos, Emre*

Sections Authored: *Results and Discussion and Conclusion*

Writing Team Number: 5

Tuesday 12:00 – 1:00 pm

Submission Date: *6 April 2024*

Introduction:

In the multifaceted field of engineering, the study and application of materials under various stress conditions plays a pivotal role in designing and enhancing the resilience of structures and components. This lab report introduces a focused investigation into the behavior of materials subjected to stress and strain, employing the principle of photoelasticity to explore the distribution and intensity of stresses. The primary purpose of this lab is to demonstrate the utility and precision of photoelastic techniques in stress analysis, providing insights that are crucial for predicting material behavior under load.

The experiments conducted utilize two types of materials: a polycarbonate used in a photoelastic model of a C-shaped semicircular ring and an aluminum plate specimen. These materials were chosen for their distinct mechanical and optical properties, facilitating a comprehensive study of stress distribution patterns when subjected to external forces. Polycarbonate, known for its birefringent (double refraction) nature, allows for the visualization of stress patterns in a transmission polariscope setup. In contrast, aluminum, with its high strength and non-birefringent characteristics, is analyzed using a birefringent coating in a reflection polariscope arrangement, highlighting the versatility of photoelasticity in materials testing.

The lab comprises two main experiments. The first employs a transmission polariscope to analyze the stress separation method on the photoelastic model, aiming to map the tangential stress along its free surfaces. This experiment underscores the relationship between the fringe patterns observed and the stress magnitude, utilizing the stress-optic law to quantify these stresses. The second experiment utilizes a reflection polariscope to examine an aluminum tensile plate with a central hole, focusing on the stress distribution and concentration factors around this discontinuity. This setup illustrates the impact of geometric irregularities on stress fields, a critical consideration in materials engineering. Measurements and data analysis in this lab involve capturing and interpreting the isochromatic fringes that represent regions of constant stress difference, translating these optical phenomena into quantifiable stress distributions. This process not only demonstrates the practical application of photoelasticity but also reinforces the theoretical principles of stress and strain analysis. Through meticulous data collection, involving digital photography and specialized polariscopic equipment, the experiments provide a detailed comparison between experimental results and theoretical predictions, emphasizing the accuracy and reliability of photoelastic methods in engineering applications.

The learning objectives of this lab encompass a deeper understanding of the stress-optic law and its application in real-world materials testing. Technically, the lab aims to equip students with the ability to conduct photoelastic analysis, interpret fringe patterns, and understand the implications of stress concentration factors in design and analysis. These objectives align with the broader goal of preparing future engineers with the knowledge and skills to assess material behavior under stress accurately, ensuring the safety and reliability of engineering solutions.

In summary, this lab report delves into the critical examination of stress distribution within materials under specific loading conditions, employing photoelasticity to bridge theoretical knowledge with practical application. Through detailed experiments on selected materials, this investigation not only illuminates the internal stress patterns that dictate material behavior but also provides a robust framework for analyzing and interpreting these patterns, contributing to the broader field of materials engineering.

Theory:

The theoretical foundation of the experiments conducted is rooted in the principles of photoelasticity, stress/strain analysis, and the constitutive relations that govern the behavior of materials under load. This section will delve into these aspects, providing a descriptive summary that contextualizes the equations and concepts in relation to the experimental techniques and data analysis conducted.

Wave Theory of Light

The Wave Theory of Light is a fundamental concept in the field of optics, particularly instrumental in understanding phenomena such as interference, diffraction, and polarization. This theory posits that light can be described as a wave, consisting of oscillating electric and magnetic fields perpendicular to each other and to the direction of propagation.

Electromagnetic Theory:

At the heart of the wave theory of light is the electromagnetic theory, which describes light as electromagnetic waves comprising electric and magnetic vector fields. These fields are in phase, perpendicular to each other, and propagate at right angles to the direction of light travel. The relationship between the wavelength (λ) and frequency of light (f), along with its velocity (c), is given by the equation:

$$c = \lambda f \quad (1)$$

In the context of photoelasticity, light's wave nature is crucial for analyzing stress and strain in materials using optical methods.

Light Sources and Wave Equation:

In experimental stress analysis, both monochromatic and white light sources are utilized. Monochromatic light, with a single wavelength, is essential for generating clear, interpretable interference patterns, whereas white light, consisting of a continuous spectrum of wavelengths, helps in identifying fringe orders in photoelastic analysis. The wave equation:

$$u = f(x - vt) + g(x + vt) \quad (2)$$

mathematically describes the propagation of light waves, where u represents the magnitude of the light vector, x the position, v the velocity of propagation, and t is time.

Superposition and Polarization:

The principle of superposition allows for the analysis of complex wave interactions, as seen in photoelasticity, where stress-induced birefringence causes light waves to split into components with different velocities. When these components recombine, they can produce patterns of constructive and destructive interference, leading to photoelastic fringes that are direct visual representations of stress distribution. Polarization, a property of light waves indicating the orientation of their oscillations, plays a critical role in photoelasticity. Light can be polarized linearly, circularly, or elliptically, with each form having distinct characteristics based on the relative phase differences between the electric field components. Linear polarizers and wave plates are optical tools used to analyze and manipulate the polarization state of light, enabling the study of stress and strain in transparent materials.

Photoelasticity and Practical Applications:

Photoelasticity is a technique that exploits the wave nature of light to investigate the mechanical behavior of materials under stress. By observing the patterns of polarized light transmitted through stressed materials, researchers can deduce the distribution of internal stresses and strains. This method is particularly valuable in experimental stress analysis, where it provides a non-destructive means to visualize and measure the effects of mechanical loads on physical objects. The wave theory of light, with its comprehensive explanation of light's behavior as a wave, including phenomena such as interference and polarization, serves as the foundation for photoelasticity. This theoretical framework not only deepens our understanding of light's nature but also enables practical applications in engineering, physics, and materials science, demonstrating the profound impact of wave theory on technology and research.

Optical Elements Conditioning Light

Optical elements serve as the bedrock of photoelasticity, a sophisticated experimental technique employed for the analysis of stress and strain within various materials. Central to this technique are polarizers and wave plates, which intricately manipulate the properties of light to unveil hidden stress patterns through the phenomenon of birefringence when examined under polarized light conditions. This comprehensive exploration delves into the intricate roles these optical components play, their strategic configurations within polariscopes, and, more specifically, the nuanced configurations of polarizers and wave plates in series, as elaborated upon in advanced studies of photoelasticity.

At the heart of photoelastic analysis lies the polariscope, an instrument embodying precision through its array of optical elements, including but not limited to linear polarizers and a spectrum of wave plates. These components are pivotal in modulating the polarization state of light, allowing for a meticulous examination of the internal stress dynamics within transparent materials. The intricacies of polariscope configurations are vast, with each setup tailored to elucidate specific aspects of stress within the test material.

Classification of Polariscope Configurations:

Polariscopes have two principal configurations, plane and circular. Each configuration is adept in its right, catering to distinct analytical needs in the realm of stress analysis.

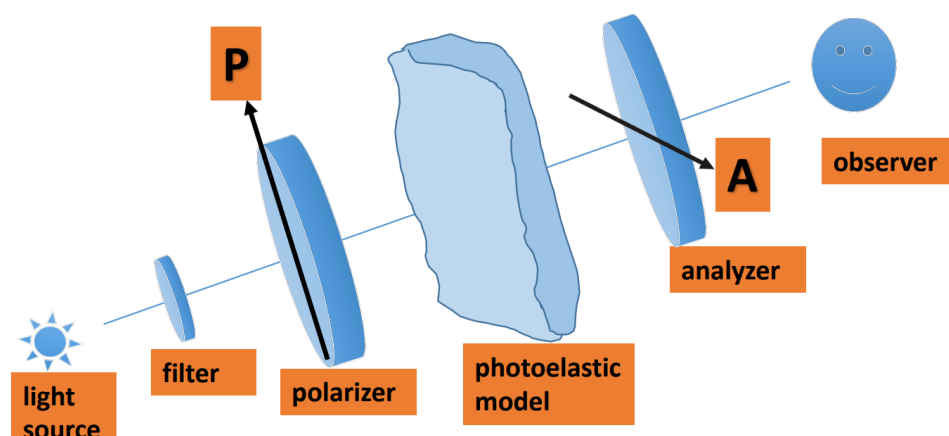


Figure 1. The Configuration of Plane Polariscope

Plane Polariscope Configuration: This setup, shown in Figure 1, is remarkably efficient at uncovering the intricate fringe patterns that emerge as direct manifestations of stress concentrations within materials. The utility of linear polarization cannot be overstated, as it facilitates the unambiguous observation of

isochromatic and isoclinic fringes. These fringes serve as crucial indicators, offering a qualitative window into the orientations and magnitudes of stresses at play. The Polarizer and the Analyzer are perpendicular to each other.

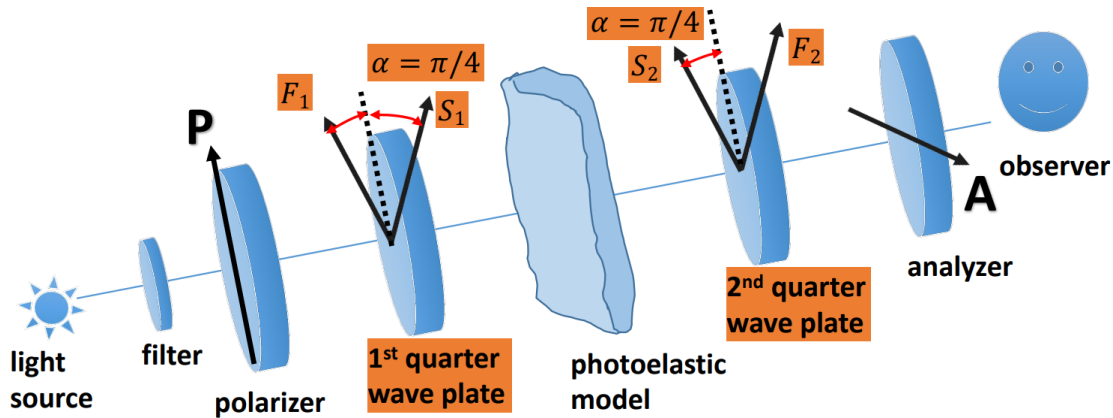


Figure 2. The Configuration of Circular Polariscopes

Circular Polariscopes Configuration: This setup, shown in Figure 2, employs a combination of linear polarizers and quarter-wave plates. The objective is to morph linearly polarized light into its circular counterpart, a transformation that brings forth significant advantages. Here the Polarizer and the Analyzer are perpendicular to each other, and so are the wave plates. The circular polariscope stands out in its ability to facilitate uninterrupted observation of isochromatic fringes, effectively disentangling them from the overlay of isoclinic lines, thus providing a pathway to quantitative stress measurement with enhanced clarity.

Wave Plates

Wave plates represent a cornerstone technology in the manipulation of light for the analysis of stress and strain in materials through photoelasticity. By introducing a phase difference between the orthogonal components of polarized light, wave plates alter their polarization state in a controlled manner. This alteration is a consequence of the wave plate's birefringent nature, which allows it to delay one component of the light relative to another, thereby changing the polarization state of the light. The essence of wave plate operation be it a quarter-wave, half-wave, or full-wave plate is encapsulated by the phase shift it imparts, a characteristic intricately linked to the material's properties and the plate's thickness.

The Principle of Birefringence:

Birefringence is the fundamental principle behind the operation of wave plates. It is a property of materials that have a different refractive index along different axes, causing light to split into two rays when it enters the material: the ordinary ray and the slower ray. Each ray travels at a different speed within the material, leading to a phase shift between them. This phase shift is critical in altering the polarization state of light.

Equations Governing Wave Plates:

The relative linear phase shift, δ , introduced by a wave plate can be quantitatively described by the equation:

$$\delta = h(n_2 - n_1) \quad (3)$$

Where, h is the thickness of the wave plate, n_2 is the refractive index for the slower ray, and n_1 is the refractive index for the ordinary ray. The relative angular phase shift, Δ , introduced by a wave plate can be quantitatively described by the equation:

$$\Delta = \frac{2\pi h}{\lambda}(n_2 - n_1) \quad (4)$$

Where, h is the thickness of the wave plate, λ is the wavelength of light in vacuum, n_2 is the refractive index for the slower ray, and n_1 is the refractive index for the ordinary ray.

These equations highlight how the phase shift is directly proportional to the thickness of the wave plate and the difference in refractive indices between the ordinary and extraordinary rays, underscoring the wave plate's ability to modify the light's polarization state through its birefringent characteristics.

Types of Wave Plates

Quarter-Wave Plates: These wave plates are designed to introduce a phase shift of

$$\delta = \frac{\lambda}{4} \quad (5), \quad \Delta = \frac{\pi}{2} \quad (6)$$

converting linearly polarized light into circularly polarized light.

Half-Wave Plates: By introducing a phase shift of

$$\delta = \frac{\lambda}{2} \quad (7), \quad \Delta = \pi \quad (8)$$

Half-wave plates rotate the polarization plane of linearly polarized light.

Full-wave plates yield a phase shift of

$$\delta = \lambda, \Delta = 2\pi$$

returning the light to its original polarization state but with a phase shift that can be used to adjust the phase of the light wave.

Incidence Phase Shift and Emergence:

The incidence phase shift refers to the initial phase difference between the ordinary ray and slowed ray as they enter the wave plate. As the rays traverse the birefringent material, their phase velocities differ, leading to a change in the phase relationship upon emergence. The emergent phase shift is critical in determining the final polarization state of the light. For instance, if the emergent phase shift is $\pi/2$, the resulting light will be circularly polarized, assuming the initial light was linearly polarized at a 45-degree angle to the wave plate's axis.

Wave plates play an indispensable role in photoelasticity, enabling the precise control of light polarization for the investigation of stress and strain in materials. Through the manipulation of birefringent properties, incidence phase shift, and emergence, wave plates provide a powerful tool for altering the polarization state of light, facilitating the detailed analysis of birefringence-induced patterns in photoelastic studies.

Polarizers and Wave Plates in Series

In the realm of experimental stress analysis, particularly within the domain of photoelasticity, the sequential combination of polarizers and wave plates plays a pivotal role. This setup, involving various configurations of polarizers (P) and wave plates (F), is essential for conditioning light to emerge either as plane polarized or circularly polarized, serving as a critical step in the visualization and analysis of stress patterns within photoelastic materials. This section aims to elucidate the theoretical underpinnings,

practical applications, and the intricate relationship between these optical elements and the experimental techniques utilized for stress and strain analysis.

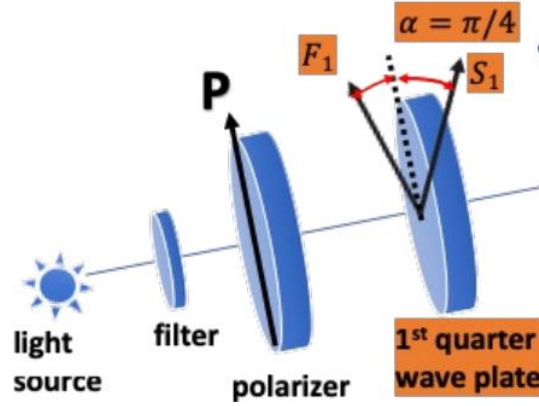


Figure 3. Zoomed Section of The Configuration of Circular Polariscopes

The configuration of polarizers and wave plates, shown in Figure 3, in series is ingeniously designed to manipulate light's polarization state, effectively facilitating the qualitative and quantitative analysis of stress within materials. The operation of this setup is governed by the principles of birefringence and polarization, where light vector (E) is modulated to achieve the desired polarization state—plane or circular—through the imposition of a relative phase difference (Δ) and the orientation angle (β) at incidence between the polarizer and the first wave plate (F_1).

Plane Polarized Light: In configurations where $\beta = 0$, implying F_1 is parallel to P , the light remains plane-polarized post-interaction with the wave plate, irrespective of the wave plate's retardation characteristics. The light vector of the emerging light (E_{out}) is described as:

$$E_{out} = k \cos(\omega t) \quad (9)$$

This simplification shows the setup's ability to maintain the light's plane polarization, proving instrumental in toggling between circular and planar polariscope configurations without altering the inherent characteristics of the wave plate.

In configurations where $\beta = \pi/2$, implying F_1 is perpendicular to P , the light vector is rotated, and light remains plane polarized. The light vector of the emerging light (E_{out}) is described as:

$$E_{out} = k \cos(\omega t - \Delta) \quad (10)$$

In this configuration, the wave plate influences light to produce retardation with respect to a wave in free space which depends on plate thickness and index of refraction.

Circularly Polarized Light: For circular polarization, the quarter-wave plate is positioned such that $\Delta = \pi/2$ and β is set to $\pi/4$, ensuring that the magnitude of the light vector remains constant magnitude, and its direction rotates with a constant angular velocity. This configuration results in light that is circularly polarized, with the direction of rotation indicating whether the light is left or right circularly polarized.

Stress Optic Law

The Stress-Optic Law is a cornerstone principle in the field of photoelasticity, offering a direct relationship between stress within a material and the optical phenomena observable through photoelastic analysis. This law underpins the experimental techniques and data analysis in stress and strain evaluation, providing a mathematical foundation for converting measured optical properties back into engineering quantities of stress and strain. Originating from the work of James Clerk Maxwell in 1853, the Stress-Optic Law articulates that changes in a material's index of refraction due to stress are linearly proportional to the applied load, and thus to the internal stresses and strains for materials behaving in a linearly elastic manner. This relationship is expressed through stress-optic coefficients, which are constants for a given material and define how the index of refraction varies with stress.

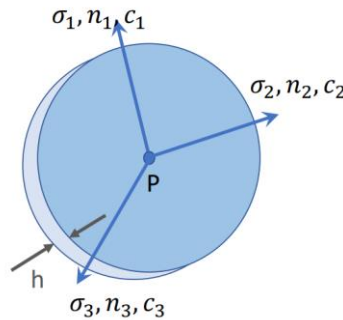


Figure 4. Principal Stresses and Refractive Indices in a Birefringent Plate

The law is mathematically represented for a photoelastic material under temporary birefringence, where the material exhibits different indices of refraction along its principal stress directions only when under load. The principal indices of refraction, n_1, n_2, n_3 align with the principal stress directions $\sigma_1, \sigma_2, \sigma_3$ respectively, shown in Figure 4.

Stress-Strain Analysis Technique

In practical applications, especially in two-dimensional (2D) stress analysis, the Stress-Optic Law facilitates the quantitative measurement of stress differences ($\sigma_1 - \sigma_2$) between the principal directions. This is achieved by considering the relative changes in the indices of refraction, which are then related back to the stresses through the stress-optic coefficient, c , a positive constant expressed in terms of Brewsters (B).

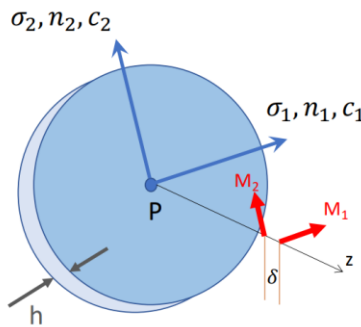


Figure 5. Wave Propagation and Phase Retardation in a Birefringent Medium

The law simplifies for 2D analysis, eliminating the need to consider the third principal stress ($\sigma_3 = 0$), and is given by:

$$n_1 - n_2 = c(\sigma_1 - \sigma_2) \quad (11)$$

The relative angular phase shift or relative retardation experienced by light as it passes through a stressed photoelastic model is directly proportional to the difference in the principal stresses, as per the equation:

$$\Delta = \frac{2\pi hc}{\lambda}(\sigma_1 - \sigma_2) \quad (12)$$

where h is the model thickness, c is the relative stress-optic coefficient, and λ is the wavelength of light used. This equation is crucial for converting optical measurements (fringe order, N , and material fringe value, f_σ) into the stress difference between the principal directions, offering a direct method for quantifying stress within the material:

$$N = \frac{\Delta}{2\pi} \quad (13), \quad f_\sigma = \frac{\lambda}{c} \quad (14), \quad \sigma_1 - \sigma_2 = \frac{\Delta \lambda}{2\pi c h} = \frac{N f_\sigma}{h} \quad (15)$$

The Stress-Optic Law provides a robust framework for understanding the relationship between mechanical stress and optical behavior in materials, enabling the detailed analysis of stress distributions and concentrations in engineering components and structures. This law, along with the techniques it supports, underscores the intrinsic connection between the physical properties of materials under stress and their optical responses, enabling engineers and researchers to visualize and quantify internal stresses non-destructively and with high precision.

For Strain:

$$\varepsilon_1 = \frac{1}{E}(\sigma_1 - \nu\sigma_2) \quad (16), \quad \varepsilon_2 = \frac{1}{E}(\sigma_2 - \nu\sigma_1) \quad (17)$$

$$\varepsilon_1 - \varepsilon_2 = \frac{1 + \nu}{E}(\sigma_1 - \sigma_2) = \frac{N f_\varepsilon}{h} \quad (18)$$

$$f_\varepsilon = \frac{1 + \nu}{E} f_\sigma \quad (19)$$

Strain Sensitive Coating

Strain-sensitive coatings, often employed in photoelasticity, provide a powerful method for analyzing stress and strain on the surface of opaque materials. These coatings, when bonded to the specimen surface, exhibit birefringence under applied stress, enabling the visualization and measurement of surface strain patterns. This section delves into the theory behind strain-sensitive coatings, elucidating their relationship with experimental techniques and data analysis in the context of stress/strain analysis. Strain-sensitive coatings work on the principle of birefringence, where the coating, upon experiencing strain, alters its refractive index in a manner proportional to the applied strain. The fundamental relationship governing the optical response of the coating to principal stress or strain differences in the specimen is encapsulated by the stress-optic and strain-optic laws.

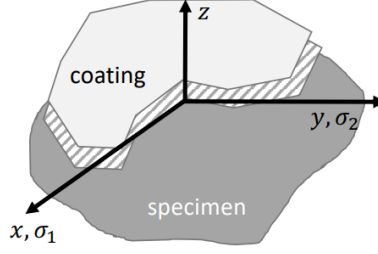


Figure 6. Strain Measurement Using Coating on a Specimen in Photoelasticity

The basic assumptions for the effective application of strain-sensitive coatings include a perfect bond between the coating and specimen, ensuring that strains are transmitted without distortion, and the principal stress difference in both the coating (c) and specimen (s) can be considered equivalent for analysis:

$$\begin{aligned}\varepsilon_1^c(x, y) &= \varepsilon_1^s(x, y) \\ \varepsilon_2^c(x, y) &= \varepsilon_2^s(x, y)\end{aligned}$$

where ε^c and ε^s denote the principal strains in the coating and specimen, respectively.

For stress and strain analysis using strain-sensitive coatings, the principal stress difference is related to the observed fringe order N in the coating, which can be expressed as:

$$(\sigma_1^s - \sigma_2^s) = \frac{E^s}{E^c} \left(\frac{1 + \nu^c}{1 + \nu^s} \right) (\sigma_1^c - \sigma_2^c) \quad (20), \quad (\sigma_1^c - \sigma_2^c) = \frac{N f_\sigma}{2h^c} \quad (21)$$

where E and ν represent the Young's modulus and Poisson's ratio of the coating (c) and specimen (s), respectively. This equation highlights the direct proportionality between the mechanical properties of the coating and the specimen, and the observable photoelastic effect. The conversion of optical measurements (fringe orders) to engineering quantities (stress or strain) involves the use of the material's fringe value f and the coating's thickness h . The principal stress difference is related to the fringe order by:

$$(\sigma_1^s - \sigma_2^s) = \frac{E^s}{E^c} \left(\frac{1 + \nu^c}{1 + \nu^s} \right) \frac{N f_\sigma}{2h^c} \quad (22)$$

This relationship allows for the direct calculation of stress differences from observed fringe patterns, providing a quantitative measure of stress on the specimen's surface. The strain-sensitive coatings provide a versatile and effective tool for surface stress and strain analysis, extending the capabilities of traditional photoelastic methods to opaque materials. Through the careful application of these coatings and the interpretation of resultant fringe patterns, engineers and researchers can gain valuable insights into the stress distributions and potential failure points within mechanical components and structures.

Materials and Methods:

This lab focused on the experiments of two, two-dimensional photoelasticity experiments. To perform these experiments, various specimens and equipment were used depending on the type of data being collected. Each experiment used a different type of polariscope with different components to capture data. Material and method selection is critical to ensure that the proper data is collected. An improper method could collect undesirable data and have an impact on the outcome of a hypothesis formed before experimentation. This section will be split up into two different sections to discuss the materials and methods used in each specific experiment.

Experiment 1:

Materials:

Experiment one explored stress magnitudes in a C-shaped semicircular specimen made from a photoelastic material, which is pictured in figure 7. The specimen was measured using a set of calipers to record the thickness, outer diameter, and the inner diameter. These measurements are shown in table 1. To explore the stress magnitudes of this specimen, it was placed inside of a transmission polariscope. The specific polariscope for this experiment was produced by Photoelastic Inc, and Pennsylvania State University serial number of 00140027, and it is shown in figure 9. This polariscope comprised of components including a white light source, polarizer plate, two-quarter wave plates, a clamping system, and an analyzer. The polarizer and analyzer are used to condition light to become plane polarized. Furthermore, the quarter wave plates are engaged to exhibit birefringence. Moreover, a monochromatic filter, shown in figure 8, was used to condition light to exhibit black and white properties instead of a full color spectrum. The last component of this experiment was a digital camera to capture images of the specimen under load for analysis to be completed.

Table 1. Dimension of the C-shape Specimen

Description	Recorded Measurement (inches)
Specimen Thickness	0.263
Inner Diameter	2.57
Outer Diameter	3.56



Figure 7. The C-Shaped specimen used in experiment 1.



Figure 8. The monochromatic filter



Figure 9. The polariscope

Methods:

To begin the experiment, the C-shaped specimen was measured using calipers to record measurements such as the specimen thickness, inner diameter, and outer diameters. Once the measurements were recorded, the specimen was placed inside the clamps of the transmission polariscope. The clamp force was measured so it could be tracked at its maximum applied force. Initially, the specimen was placed under a load of three pounds to show the zero-order fringe appeared with additional stresses in the specimen as seen in figure 10. The desired number of fringes visible was 5-6, so additional stress was applied to achieve this number of fringes [7]. To make sure the fringes were visible, the monochromatic filter was used to make the fringes more visible and ensure that accurate data was collected. The final applied force was 20 pounds, which was used later for data analysis. The first portion of this experiment was performed in the polariscope's dark field [7]. The digital camera was used to capture the stress magnitudes present on the specimen, which is depicted in figure 11. Once the data was captured, the polariscope was changed to the light field setting to capture whole order data compared to the half-order data collected in the light field setting [7]. Once all of the desired data was collected, the clamp force was reduced, and the specimen was removed from the polariscope. The images were then digitally uploaded for further analysis.

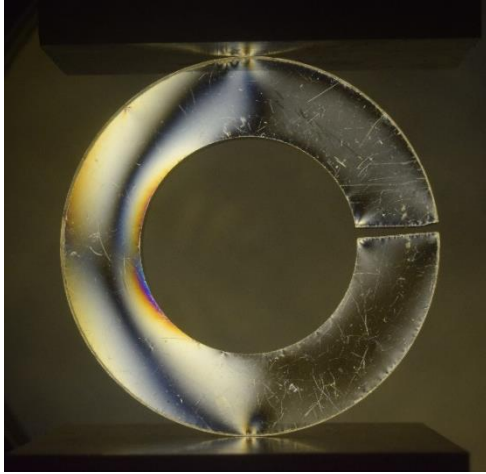


Figure 10. The zero-order fringe under initial load

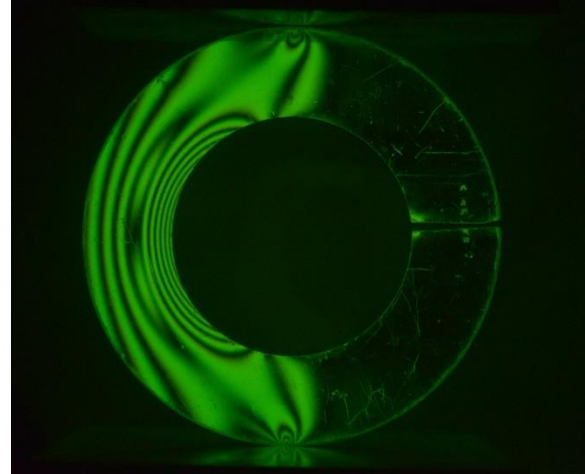


Figure 11. The dark field config under full load

Once the images were collected, they needed to be analyzed. The digital images needed to be evaluated to find angles for each fringe so theoretical stress values could be calculated later. The first step in this process was to take the light field and dark field images into the computer software Paint. In this software each image was marked with a 90° angle axis to allow for angle measurements to be recorded in the following steps. Once the axis was set, more lines were created, stemming from the origin to each fringe. Two sets were created for each light field and dark field image. The first drew lines to the inner fringes, while the second was set up for the outer fringes. Shown in Figure 12 is an example of an output from the Paint software for the outer fringes for the light field image captured during the first portion of the methods in this experiment. Next, these images were taken to another computer software called ImageJ. ImageJ allows the user to take measurements through pixel counts. Each image was uploaded into the software, and the angle measurement tool was used to record angles to each the end of each fringe. This tool allowed the previously drawn lines to be traced and used these lines to generate angle measurements. In equation 23, the only unknown left to solve for the stress in the theta direction is the radius (r). For the calculations with the inner fringes, the inner radius was used to substitute into the equation. For the outer fringes, the outer radius was used for calculations.

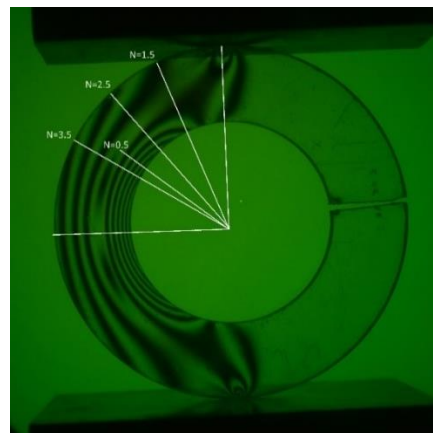


Figure 12. An annotated disk in the light field configuration

$$\sigma_{\theta} = 2A \left[3r - \frac{a^2 b^2}{r^3} - \frac{(a^2 b^2)}{r} \right] \sin(\theta) \quad (23)$$

Experiment 2:

Materials:

The second experiment of this lab explored the stress directions of the tested specimen. The specimen used for experimentation in this section of the lab was a rectangular aluminum specimen with a 1-inch diameter hole in the center, as pictured below in Figure 13. The specimen also consisted of a birefringent coating to show the stress fringes and direction on the specimen in experimentation. The dimensions of the specimen were gathered using a set of calipers, and the recorded values are shown in table 2. The specimen was placed inside of a reflection polariscope for testing shown in Figure 14. The specific polariscope used in this experiment was the Model 040 Reflection Polariscope, with a serial number of 2085, produced by the Photoelastic Division of the Measurement Group. This polariscope configuration consisted of a light source, polarizer, and analyzer. Similarly to the previous selection, the polarizer and analyzer condition light to become plane polarized. The difference in this polariscope from the first experiment, is this reflection polariscope does not have engaged quarter wave plates.



Figure 13. An image of the tested specimen

Table 2. Dimension of the Specimen with Center Hole

Description	Specimen Measurement (Inches)
Hole Diameter	1
Specimen Thickness	0.067
Coating Thickness	0.119
Width of Specimen	1.986



Figure 14. The Reflection Polariscope used for experimentation

Methods:

Before conducting testing, the specimen was measured using a set of calipers. The measured sample was then placed in the clamps of the reflection polariscope. Before applying any stress, the desired fringe amount that will not be exceeded during the experiment. Once the maximum fringe order was calculated, the polariscope was set to the dark field setting by rotating knob A [7]. Next, additional force was added while watching the number of fringes that were appearing on the specimen. At the desired number of fringes, the stress was recorded (355lbs). Since the specimen was at the desired force load, further analysis could be conducted. One piece of data needed was the Babinet Soliel compensator (N) value at each of the seven locations in the A-B directions on the specimen [7]. A dial was turned on the front lens to recenter the zero-order fringe on each of the seven locations, and the N value was recorded each time [7]. Lastly, an image was taken through the lens to further analyze. The image gathered from the digital camera, and shown in Figure 15, needed to be processed and analyzed. Once the image was uploaded, it was taken and put into ImageJ to calculate distances to the seven locations on the A-B path through pixel counts. In order to accomplish this, the pixel count was measured over the width of the specimen. This number was then divided from width dimension of the specimen in inches to record a value in the units of inches/pixels. This unit and standard could then be used to convert the other pixel counts back to distances for a radius (r value) to be recorded. The centerline of the specimen was located, and then pixel counts were measured from the center to the edge of the hole as well as the seven locations. The recorded N and r values were then plugged into equations 24 and 25 to find theoretical principal strain difference. σ_o was found using the force divided by the cross-sectional area recorded at the beginning of the experimentation. The calculated theoretical values were then compared to the experimental values, which will be shown in the results section of this report.



Figure 15. The specimen under load through the Polariscope

$$\sigma_{rr} = \frac{\sigma_o}{2} \left\{ \left(1 - \frac{a^2}{r^2} \right) * \left[\left(1 + \left(\frac{3a^2}{r^2} - 1 \right) \right) * \cos(2\theta) \right] \right\} \quad (24)$$

$$\sigma_{\theta\theta} = \frac{\sigma_o}{2} \left[\left(1 + \frac{a^2}{r^2} \right) + \left(1 + \frac{3a^4}{r^4} \right) * \cos(2\theta) \right] \quad (25)$$

Results and Discussion:

Experiment 1 Part A:

The final annotated images from the experimental testing of the semicircular ring with a C-shape geometry that was loaded under diametral compression can be viewed in Figure 16-19. These annotated images feature the fully counted fringe order in accordance with Saint-Venant's Principle including post processing of data in imageJ. This software used pixel placement and user placed markers to identify lengths and angles on the specimen images. Unfortunately, some fringes were slightly incoherent and resulted in being omitted, these fringes were usually when $N=1$ or $N=1.5$ in both the light and dark field configurations. This likely occurred due to the rudimentary nature of the test and a well worn specimen. There was no specified load applied in the protocol, the only criteria was to visually estimate the generation of 6 fringes which led to some lack of precision in the data collection phase.

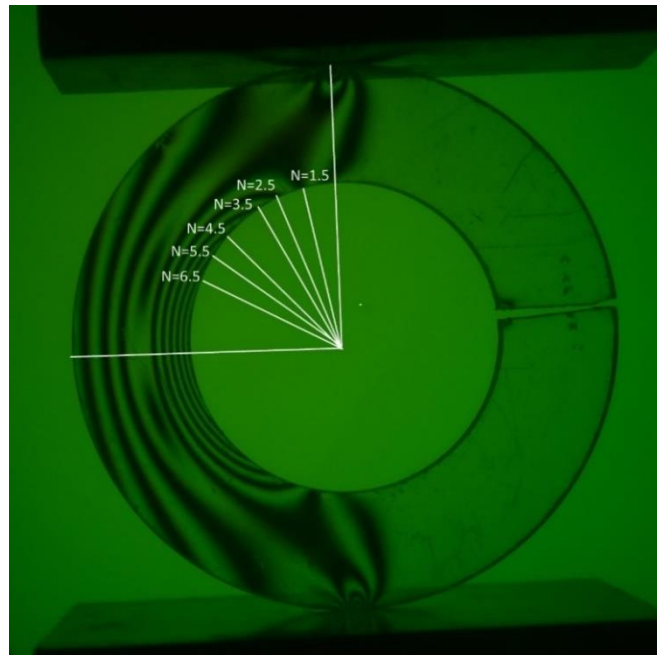


Figure 16. Annotated inner boundary in the light field configuration

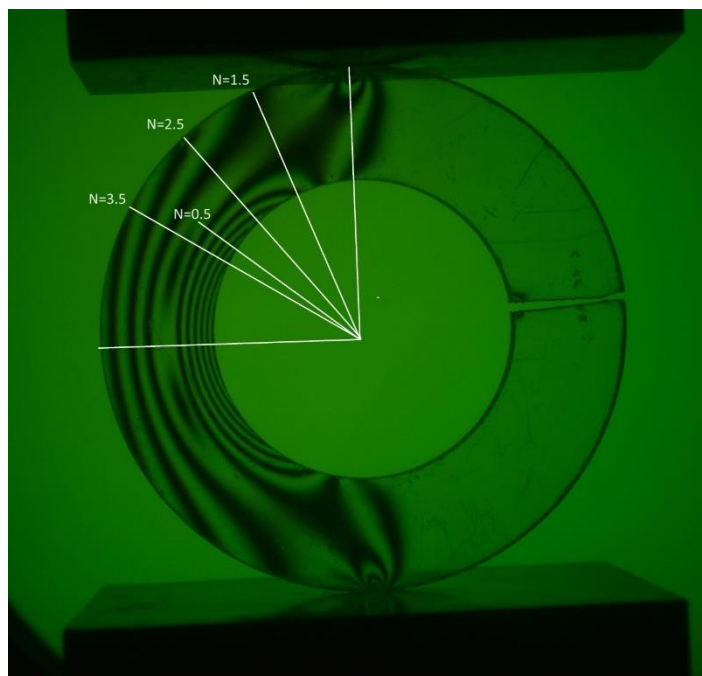


Figure 17. Annotated outer boundary in the light field configuration

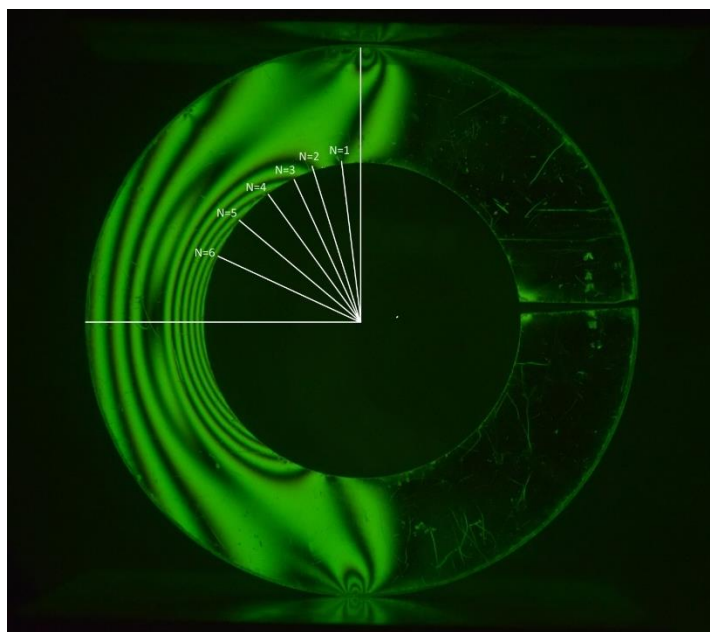


Figure 18. Annotated inner boundary in the dark field configuration

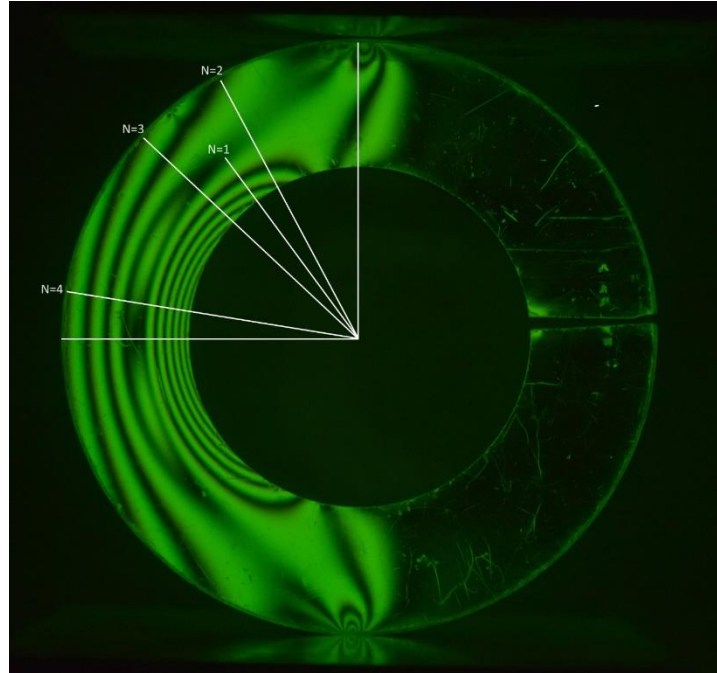


Figure 19. Annotated outer boundary in the dark field configuration

Following image analysis, calculations needed to be completed to tabularize the stress magnitudes from the resulting angular data. The complete workup of the tabularized results can be seen in Tables 3-6. The calculation for both experimental and theoretical stress magnitude required a different formula. The process for these calculations can be seen under the sample calculations for experiment 1A in the appendix. Furthermore, the data visualization of the relationships between stress magnitude data and angular position can be observed in graphs featured in Figures 20-21.

Table 3: Principal Stresses along Inner Boundary (Whole Order)

Angular θ Position ($^{\circ}$)	Fringe Order (N)	Stress Magnitude		
		Experimental (psi)	Theoretical (psi)	Difference (%)
0	0	0	0	0
6.73	1	-152.09	-59.1970189	156.9238
17.1	2	-304.18	-148.5297396	104.7957
25.309	3	-456.27	-215.944682	111.292
35.983	4	-608.37	-296.788998	104.9823
49.938	5	-760.46	-386.6034468	96.70189
63.733	6	-912.55	-458.3039029	99.11406

Table 4: Principal Stresses along Inner Boundary (Half Order)

Angular θ Position ($^{\circ}$)	Fringe Order (N)	Stress Magnitude		
		Experimental (psi)	Theoretical (psi)	Difference (%)
11.389	1.5	-228.1368821	-100.9219262	55.76256
21.069	2.5	-380.2281369	-183.7280667	51.67952

27.753	3.5	-532.3193916	-237.9885341	55.29215
43.468	4.5	-684.4106464	-351.5950567	48.62806
52.504	5.5	-836.5019011	-405.4863305	51.52595
61.168	6.5	-988.5931559	-447.7225702	54.71114

Table 5: Principal Stresses along Outer Boundary (Whole Order)

Angular θ Position (°)	Fringe Order (N)	Stress Magnitude		
		Experimental (psi)	Theoretical (psi)	Difference (%)
36.406	1	-152.0912548	215.1005932	241.4286
27.833	2	-304.1825095	169.2149613	155.6294
46.625	3	-456.2737643	263.4377071	157.7368
80.958	4	-608.365019	357.9216336	158.8334

Table 6: Principal Stresses along Outer Boundary (Half Order)

Angular θ Position (°)	Fringe Order (N)	Stress Magnitude		
		Experimental (psi)	Theoretical (psi)	Difference (%)
51.328	0.5	-76.04562738	282.9584673	472.0904
20.482	1.5	-228.1368821	126.8173767	155.5883
39.23	2.5	-380.2281369	229.2104659	160.2824
57.309	3.5	-532.3193916	305.0155894	157.2994

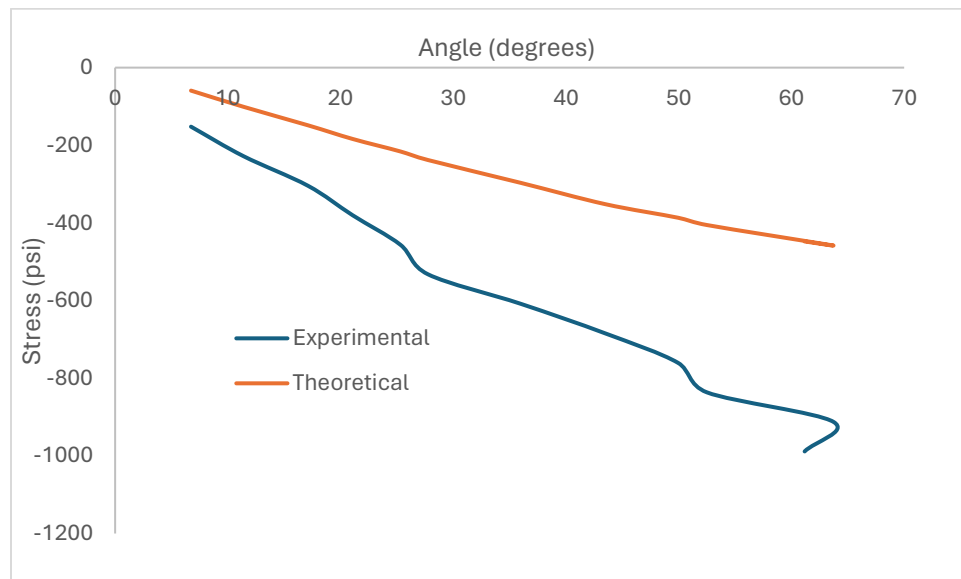


Figure 20. Inner boundary relationship between stress and angle

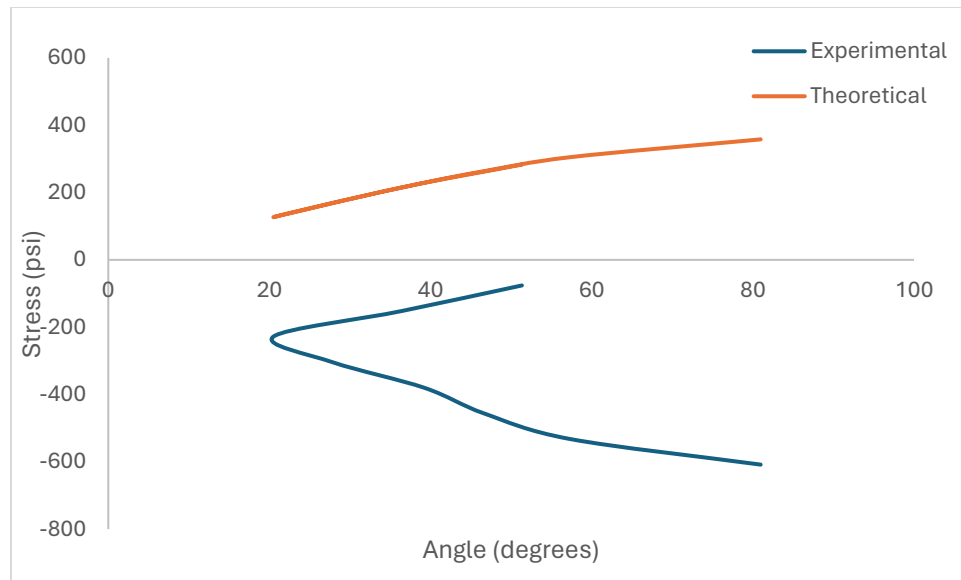


Figure 21. Outer boundary relationship between stress and angle

As observed in both the tables and figures, there are significant differences in trends between the relationship between the outer boundary's relationship to stress and the inner boundaries relationship to stress. For the inner boundary's relationship, as the angle increases, the magnitude of the stress grows in magnitude in the compressive nature. This relationship stands not only for theoretical data, but also for theoretical data. Simultaneously, for the outer boundary's relationship, as the angle increases, the magnitude of the stress also grows. In our theoretical data, this magnitude grew in the tensile direction while in our experimental data this magnitude grew in the compressive direction. Furthermore, when observing the graph in Figure 21, you can see why the first fringe orders in the outer boundary should be omitted as they cause a non-linear relationship between angle and stress. The experimental data should follow the similar trend of the theoretical data, which it does, just after the first fringes of $N=0.5$ and $N=1$.

Throughout this experiment, as seen in Tables 3-6, it is important to note that there was a large percentage of difference between the theoretical and experimental results. This could be due to a variety of factors such as the positioning of the camera not giving accurate measurements of the angle directly correlating to incorrect pixel counting using ImageJ. However, the graphs in figure 20 & 21 exhibit similar shapes which indicate there was a solid relationship between the theory discussed and the results gathered in the lab.

Experiment 1 Part B:

The second portion of the experiment relied on finding the maximum principal stress along the horizontal axis of symmetry which was done only in the dark field configuration. The goal behind this was to discover the principal stress maximum magnitude as well as the finite location along the specimen. Table 6 shows the tabularized results for the principal stresses along the horizontal axis of symmetry and using this table, the conclusion can be drawn that the maximum experimental principal stress was found at the position of 1.315 inches from the center of the specimen which yielded a theoretical stress magnitude of 203.26 psi and an experimental stress magnitude of 912.55 psi. While there is still a large percentage

difference of %348.96 between the two, they both accurately represent the maximum values of stress magnitude in the 6th fringe of their represented categories.

Table 6: Principal stresses along horizontal axis of symmetry

Position (inches)	Fringe Order	Stress Magnitude		
		Experimental (psi)	Theoretical (psi)	Difference (%)
1.694	0	0	0	0
1.624	1	-152.09	-59.1970189	156.9238
1.545	2	-304.18	-148.5297396	104.7957
1.479	3	-456.27	-215.944682	111.292
1.424	4	-608.37	-296.788998	104.9823
1.366	5	-760.46	-386.6034468	96.70189
1.315	6	-912.55	-458.3039029	99.11406

Experiment 2 Part A:

In the second portion of the experiment, a rectangular specimen with an extruded circular cut in the center was the focus of the study. Prior to exposing this specimen to any load, the maximum desired fringe order needed to be calculated as seen in equation 26. Plugging in the given values yielded a maximum fringe order of 2.03 meaning the specimen needed to be loaded until roughly 2 fringe orders appeared as seen in figure 15.

$$N_{max} = C_c C_s \sigma_{ys} \quad (26)$$

Following this, a Babinet Soliel Compensator was utilized to evaluate the specimen's fringe order roughly around every 0.0625 inches to the right of position A on the specimen. The resulting data was utilized to calculate principal strain differences on both the coating and specimen that were then in turn utilized to calculate principal stress differences as seen in the sample calculations in the appendix. The tabularized data of the experiment can be seen in table 7.

Table 7: Principal Stress & Strain Differences along specimen

Position (Inches)	Babinet Soliel Compensator Value, N	Principal Strain Differences (in/in)		Specimen Principal Stress Difference ($\sigma_1 - \sigma_2$) ^s (psi)	
		($\varepsilon_1 - \varepsilon_2$) ^c	($\varepsilon_1 - \varepsilon_2$) ^s	Experimental	Theoretical
0.561163	2.93	0.001861	0.001972	15284.92	2667.929
0.625827	2.22	0.00141	0.001494	11581.07	5001.961842
0.686111	1.94	0.001232	0.001306	10120.39	3868.586526
0.756258	1.8	0.001143	0.001211	9390.055	3280.242257
0.82202	1.74	0.001105	0.001171	9077.053	2892.304037
0.872439	1.69	0.001073	0.001137	8816.218	2688.81952
0.934913	1.62	0.001029	0.00109	8451.05	2593.77101

Utilizing the data visualization of figures 22-24, conclusions can be drawn from the shape of the figures as well as the numerical trends of the figures. In particular, as the position along the horizontal axis draws closer to the center of the circle defined as x=0, Babinet Soliel Compensator value, experimental stress difference, and theoretical stress differences reach their maximum values. It is also important to note that

the changes further away from the center of the circle are less significant than the changes closer to the center of the circle. This is due to the fact that as the position draws closer to the hole, the stress concentration factor increases exponentially which is represented in the exponential shape of the increases in all 3 of the graphs.

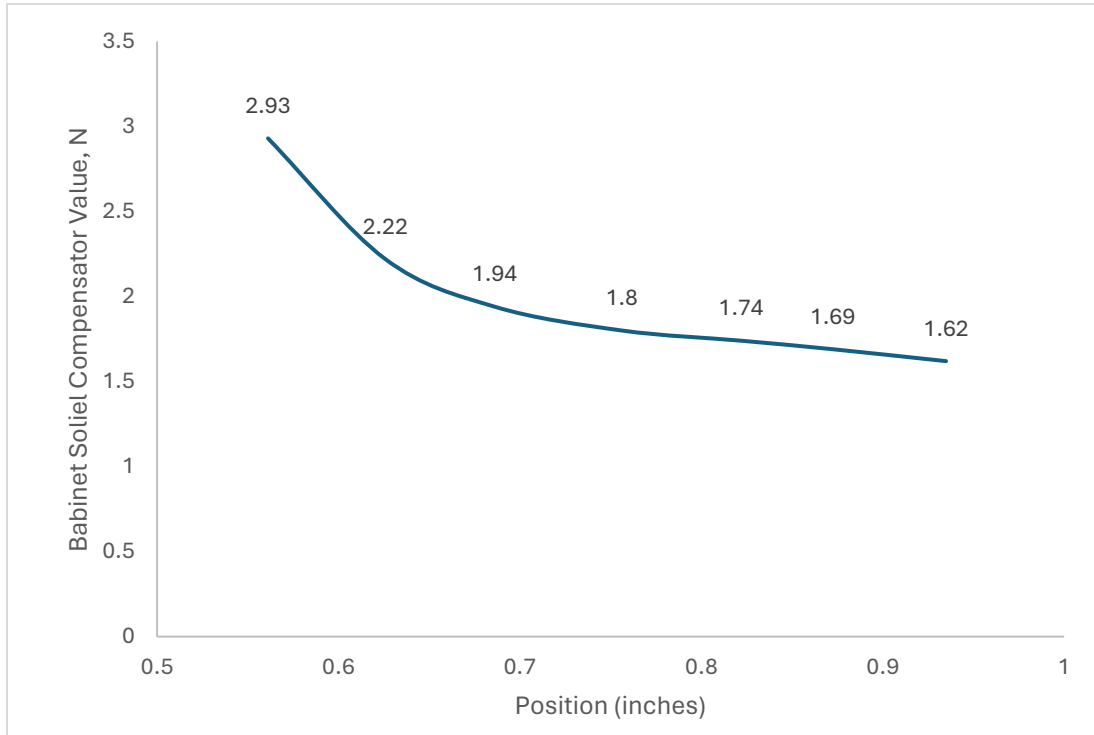


Figure 22. Position vs. babinet soliel compensator value graph

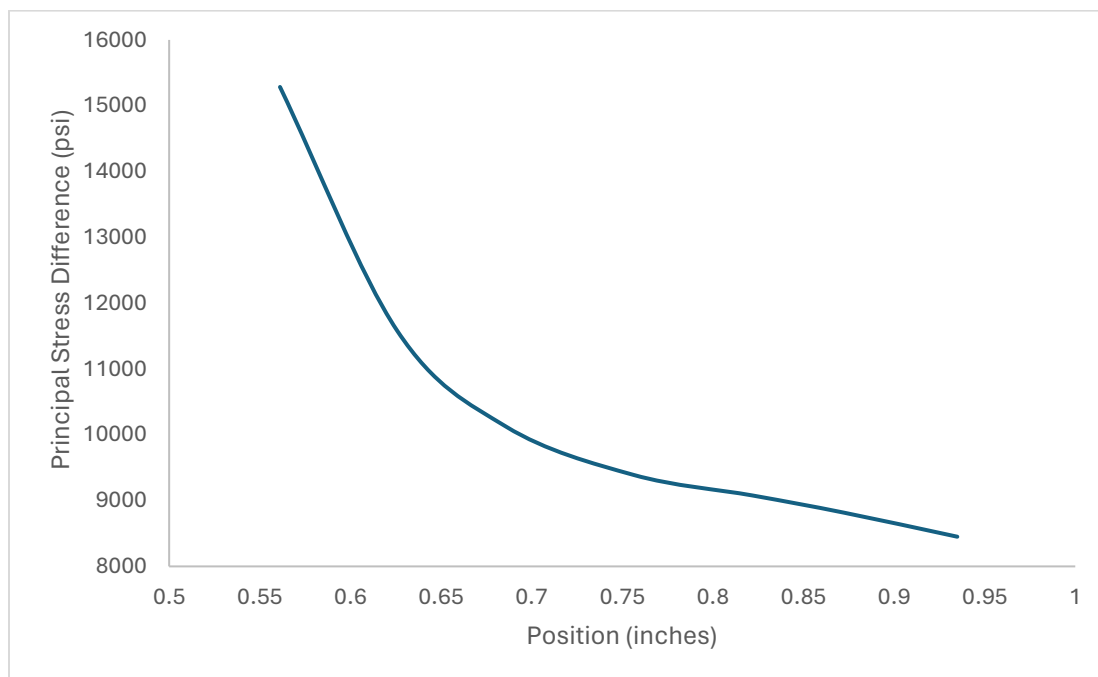


Figure 23. Position vs. Experimental stress difference graph

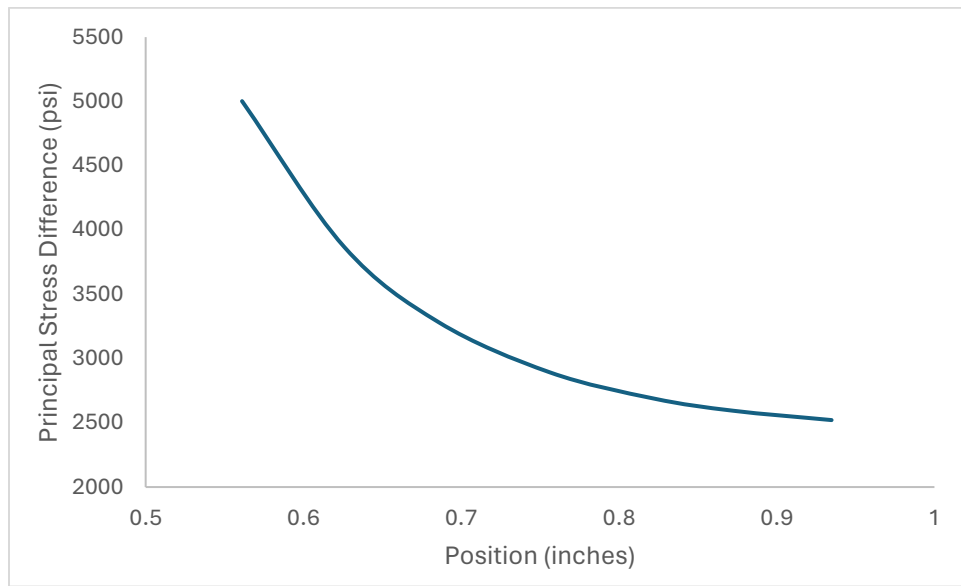


Figure 24. Position vs. Theoretical stress difference graph

Part B:

In the second portion of the experiment, the stress concentration factor at the boundary of the hole along path AB was determined experimentally. This was done to further reinforce the trend exposed in part A where the stress differences and compensator values increased exponentially as they approached the center of the hole. The Experimental stress concentration factor at the boundary was determined to be 5.73 as seen in the sample calculation in the appendix. The Theoretical stress concentration factor at the boundary was determined to be 2.16 as seen in the sample calculation in the appendix. This trend further reinforces ideas from prerequisite courses between the relationship of stress concentration factor and position seen in figure where stress will increase as you approach the drilled hole in Figure 25.

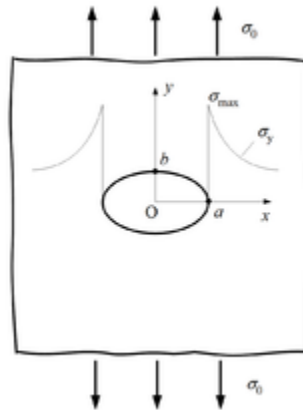


Figure 25. Stress Concentration of plate with drilled circular hole

Conclusion:

Utilizing 2-D photoelasticity techniques, this study successfully extracted a full field of data from a free form C-shaped specimen as well as a rectangular plate with a drilled central hole. The main operating principles behind the photoelastic techniques were general relationships between stress and strain as well as the optomechanical property referred to as birefringence. Combining these relationships with the stress optic law allowed quantities such as fringe order, fringe factors, and birefringent coating properties to yield successful experimental data. However, this did come with a large set of pros and cons. This methodology was phenomenal for gathering visual understanding of how stress interacts in a specimen, however the accuracy of the methodology left a lot to be desired. There were large discrepancies between the percent differences of experimental and theoretical values despite having similarly shaped trends when graphed. This could potentially be due to a variety of factors such as lackluster image post processing as well as inaccurate imaging due to the lack of precision that a tool like a tripod would have increased. Overall, some of the key takeaways for this lab were that as angles approached the horizontal axis of symmetry, there was an increase in stress magnitude for the C-shape specimen. Furthermore, the highest amounts of stresses were located at the inner and outer boundaries of the C-shape specimen. Regarding the rectangular plate with a drilled center hole, the largest takeaway is that as position draws closer to the hole on the horizontal x axis, the stress concentration will grow. This trend was observed in three separate graphs for both experimental data, theoretical data, and compensator data. However, similarly to the C-shape specimen there were large discrepancies between the magnitudes of data and not their actual trend. The similar reasons discussed previously are likely causes for this resounding gap in magnitude. This lab was extremely insightful and yielded a concrete understanding of 2-D photoelastic techniques.

Applications:

Photoelasticity plays a major role in a variety of engineering disciplines. Being able to understand principal stress magnitudes and directions can give critical insights to challenges in various engineering problems across disciplines. One discipline that can use these principles is biomedical engineering. In biomedical engineering, photoelasticity can be used to explore experiments such as testing new materials. For example, one real world application is the use of photoelastic testing to help develop a material with material properties similar to human skin tissue.

Scientists and engineers previously were struggling to explore the interaction between needles and skin tissue. Surrogate material needed to be developed to exhibit similar material properties to skin [8]. The similar material properties ensure that testing provides applicable data to what would be seen in human skin tissue that is not as accessible to test as a specimen through a polariscope. The main material properties needed for this experiment were the viscoelastic nature and the approximate elastic modulus [8]. The last requirement was that the material was transparent and would exhibit temporary birefringence [8].

As the team of scientists and engineers developed the material, they used a base material of konjac glucomannan, which is an amorphous polymer [8]. This gel has had studies performed before that show that this gel does not crack when punctured, unlike more conventional gels. This type of resistance to a puncture is also exhibited in skin tissue, which made this a desirable property of the gel. To form the testing material, the gel powder was mixed with water, and after sitting for twenty-four hours, the

mixture heated for one hour and placed into a mold [8]. Once the mold cooled, it was removed and cooled further in a refrigerated setting until it was time for testing [8].

Now that the potential surrogate material was created, it became time to test the material. The material was put through a variety of tests. The first two tests were simple tensile and compression tests to develop engineering stress versus engineering strain curves to compare to that of skin tissue. The main test came from photoelasticity. The specimen was placed in a polariscope and elongated to a designated strain of 20mm [8]. A Stress Photonics software was used to record the fringe order and retardation while the specimen was being stretched under a tensile force as seen in figure 26.

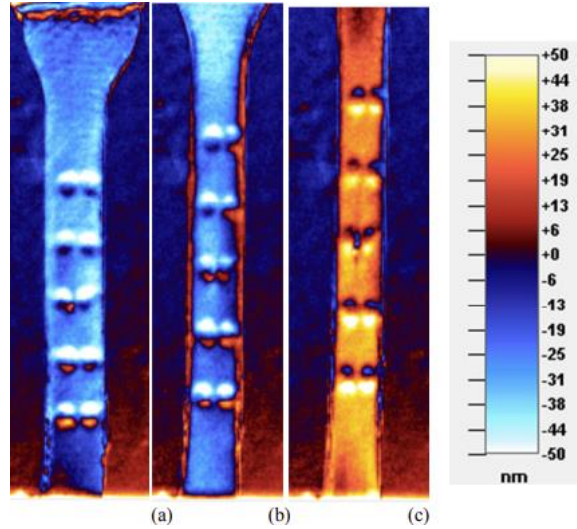


Figure 26. The fringe order and retardation results from experimentation

Once the data was collected, equation 27 was used to develop a relationship between fringe order (N) and retardation (δ). Equation 28 was then used to find the strain optic coefficient (f_ϵ).

$$N = \frac{\delta}{2\pi} \quad (27)$$

$$f_\epsilon = \frac{(\epsilon_2 - \epsilon_1) * 2\pi t}{\delta} \quad (28)$$

When all the data was analyzed, it became clear that this material was a potential fit for a surrogate material for skin tissue. One of the main findings was that the strain optic coefficient will produce low fringe orders. This was a critical finding because future tests will be conducted using a grey field polariscope that functions best with fringe orders under 2.5 [8]. The use of photoelasticity played a major role in this testing, and it will continue to play a critical part in testing the surrogate material in the future. Photoelasticity has a variety of applications, and exploring surrogate material was only one example of how it can be applied in a biomedical engineering setting.

References:

- [1] R. Hamilton. “Photoelasticity 1” *Pennsylvania State University* (2024)
<https://psu.instructure.com/courses/2310697/assignments/syllabus>
- [2] R. Hamilton. “Photoelasticity 2” *Pennsylvania State University* (2024)
<https://psu.instructure.com/courses/2310697/assignments/syllabus>
- [3] R. Hamilton. “Photoelasticity 3” *Pennsylvania State University* (2024)
<https://psu.instructure.com/courses/2310697/assignments/syllabus>
- [4] R. Hamilton. “Photoelasticity 4” *Pennsylvania State University* (2024)
<https://psu.instructure.com/courses/2310697/assignments/syllabus>
- [5] R. Hamilton. “Photoelasticity 5” *Pennsylvania State University* (2024)
<https://psu.instructure.com/courses/2310697/assignments/syllabus>
- [6] R. Hamilton. “Photoelasticity 6” *Pennsylvania State University* (2024)
<https://psu.instructure.com/courses/2310697/assignments/syllabus>
- [7] Lab 2: Applied 2D Photoelastic Analysis: EMCH 402, Section 001: Stress Analysis (22411--UP---P-EMCH---402-----001-). (2020). Retrieved April 6, 2024, from Instructure.com website:
https://psu.instructure.com/courses/2310697/pages/lab-2-applied-2d-photoelastic-analysis?module_item_id=41001558
- [8] Falconer, S. E., Taylor, Z. A., & Tomlinson, R. A. (2019). Developing a soft tissue surrogate for use in photoelastic testing. *Materials Today: Proceedings*, 7, 537–544.
<https://doi.org/10.1016/j.matpr.2018.12.005>

Appendix:

Experiment 1 Calculations

Experimental Stress Magnitude:

$$\sigma_2 = -\frac{Nf_\sigma}{h}$$

Where:

N = Fringe Order

h = Height of Specimen

f_σ = Material Stress Fringe Coefficient

Let:

N = 2

h = 0.263 inches

$f_\sigma = 40 \text{ lb/in}$

Therefore:

$$\begin{aligned}\sigma_2 &= -\frac{2 * 40}{0.263} \\ \sigma_2 &= -304.18 \text{ psi}\end{aligned}$$

Theoretical Stress Magnitude:

$$\begin{aligned}2A &= \frac{P}{a^2 - b^2 + (a^2 + b^2) * \ln\left(\frac{b}{a}\right)} \\ \sigma_\theta &= 2A \left[3r - \frac{a^2 b^2}{r^3} - \frac{(a^2 b^2)}{r} \right] \sin(\theta)\end{aligned}$$

Where:

a = Inner Radius

b = Outer Radius

P = Applied Load

r = Radial Measurement From Center

θ = Tangential Direction

Let:

a = 1.285 inches

b = 1.78 inches

P = 3 lbs

r = 1.32663 inches

$\theta = 17.1^\circ$

Therefore:

$$\begin{aligned}2A &= \frac{3}{1.285^2 - 1.78^2 + (1.285^2 + 1.78^2) * \ln\left(\frac{1.78}{1.285}\right)} \\ 2A &= 56.26 \\ \sigma_\theta &= 56.26 \left[(3 * 1.32663) - \frac{1.285^2 1.78^2}{1.32663^3} - \frac{(1.285^2 1.78^2)}{1.32663} \right] \sin(17.1) \\ \sigma_\theta &= -148.529 \text{ psi}\end{aligned}$$

Experiment 2 Calculations

Principal Strain Differences:

$$\begin{aligned}(\varepsilon_1 - \varepsilon_2)^c &= N * F \\(\varepsilon_1 - \varepsilon_2)^s &= F_{CR} * (\varepsilon_1 - \varepsilon_2)^c \\F_{CR} &= \left(1 + \frac{h^c E^c (1 + \nu^s)}{h^s E^s (1 + \nu^c)}\right)\end{aligned}$$

Where:

N = Babinet Soliel Compensator Value

F = material “f-value”

h^c = Height of Coating

E^c = Young’s Modulus of Coating

ν^c = Poisson’s Ratio of Coating

h^s = Height of Specimen

E^s = Young’s Modulus of Specimen

ν^s = Poisson’s Ratio of Specimen

F_{CR} = Reinforcement Correction Factor

Sample Calculation:

Let:

$$N = 2.93$$

$$F = 635 \mu\epsilon/\text{fringe}$$

$$h^c = 0.119 \text{ inches}$$

$$E^c = 3690 \text{ Ksi}$$

$$\nu^c = 0.38$$

$$h^s = 0.067$$

$$E^s = 10 \text{ Msi}$$

$$\nu^s = 0.29$$

$$F_{CR} = 1.05977 \text{ (from calculation)}$$

Therefore:

$$(\varepsilon_1 - \varepsilon_2)^c = 2.93 * 0.00635$$

$$(\varepsilon_1 - \varepsilon_2)^c = \mathbf{0.001861 \text{ in/in}}$$

$$F_{CR} = \left(1 + \left(\frac{(0.119)(360,000)(1 + 0.29)}{(0.067)(10^6)(1 + 0.38)}\right)\right)$$

$$\mathbf{F_{CR} = 1.05977}$$

$$(\varepsilon_1 - \varepsilon_2)^s = 1.05977 * 0.001861$$

$$(\epsilon_1 - \epsilon_2)^s = 0.001972$$

Principal Stress Differences:

Experimental:

$$(\sigma_1 - \sigma_2)^s = \left(\frac{E^s}{(1+\nu^s)} \right) * (\epsilon_1 - \epsilon_2)^s$$

Where:

E^s = Young's Modulus of Specimen

ν^s = Poisson's Ratio of Specimen

$(\epsilon_1 - \epsilon_2)^s$ = Principal Strain Difference

Let

$E^s = 10 \text{ Msi}$

$\nu^s = 0.29$

$(\epsilon_1 - \epsilon_2)^s = 0.001972$

$$(\sigma_1 - \sigma_2)^s = \left(\frac{10^6}{1 + 0.29} \right) * (0.001972)$$

$$(\sigma_1 - \sigma_2)^s = 15284.92 \text{ psi}$$

Theoretical:

$$(\sigma_1 - \sigma_2)^s = (\sigma_{rr} - \sigma_{\theta\theta})$$

$$\sigma_{rr} = \frac{\sigma_o}{2} \left\{ \left(1 - \frac{a^2}{r^2} \right) * \left[\left(1 + \left(\frac{3a^2}{r^2} - 1 \right) \right) * \cos(2\theta) \right] \right\}$$

$$\sigma_{\theta\theta} = \frac{\sigma_o}{2} \left[\left(1 + \frac{a^2}{r^2} \right) + \left(1 + \frac{3a^4}{r^4} \right) * \cos(2\theta) \right]$$

$$\sigma_o = \frac{F}{A}$$

$$A = w * h^s$$

Where:

a = Radius of Hole

r = Length to Point of Interest

θ = Angle of Measurement

F = Load on Specimen

A = Cross Sectional Area of Specimen

Sample Calculation:

Let:

$h^s = 0.067 \text{ inches}$

$w = 1.986 \text{ inches}$

$a = 0.48 \text{ inches}$

$r = 0.5611 \text{ inches}$

$\theta = 0^\circ$

$F = 355 \text{ lbs}$

Therefore:

$$A = 0.067 * 1.986$$

$$A = 0.133062 \text{ in}^2$$

$$\sigma_o = \frac{355}{0.133062}$$

$$\sigma_o = 2667.929 \text{ psi}$$

$$\sigma_{rr} = \frac{2667.929}{2} \left\{ \left(1 - \frac{0.48^2}{0.5611^2} \right) * \left[\left(1 + \left(\frac{3 * 0.48^2}{0.5611^2} - 1 \right) \right) * \cos(0) \right] \right\}$$

$$\sigma_{rr} = 785.41687 \text{ psi}$$

$$\sigma_{\theta\theta} = \frac{2667.929}{2} \left[\left(1 + \frac{0.48^2}{0.5611^2} \right) + \left(1 + \frac{3 * 0.48^4}{0.5611^4} \right) * \cos(0) \right]$$

$$\sigma_{\theta\theta} = 5787.378716 \text{ psi}$$

$$(\sigma_1 - \sigma_2)^s = 5787.378716 - 785.41687$$

$$(\sigma_1 - \sigma_2)^s = 6572.796 \text{ psi}$$

Experimental Stress Concentration Factor

$$K_t = \frac{\sigma_{max}}{\sigma}$$

$$\sigma = \frac{F}{A}$$

Where:

K_t = Stress Concentration Factor

σ_{max} = Max Stress on the Specimen (Experiment 2 Part A)

σ = Stress due to load applied

F = Load applied to Specimen

A = Cross Sectional Area of the Specimen

$$K_t = \frac{15284}{355 / (0.067 * 1.986)} = 5.73$$

Theoretical Stress Concentration Factor

$$K_t = 3 - 3.13 \left(\frac{d}{w} \right) + 3.66 \left(\frac{d}{w} \right)^2 - 1.53 \left(\frac{d}{w} \right)^3$$

Where:

K_t = Stress Concentration Factor

d = Diameter of the hole

w = width of the specimen

$$K_t = \frac{\sigma_{max}}{\sigma}$$

$$\sigma_{max} = K_t * \left(\frac{F}{(w - d)t} \right) = 2.157 * 5373.74 = 11591.2 \frac{lb}{in^2} = 11.59 \text{ ksi}$$

$$K_t = 3 - 3.13 \left(\frac{1}{1.986} \right) + 3.66 \left(\frac{1}{1.986} \right)^2 - 1.53 \left(\frac{1}{1.986} \right)^3 = 2.157$$